INJURY BIOMECHANICS RESEARCH
Proceedings of the Forty First International Workshop

Investigation of fracture mechanisms in rib cortical bone

J. Toczyski, J. P. Donlon, S. Boruah and D. Subit
Center for Applied Biomechanics, University of Virginia

This paper has not been screened for accuracy nor refereed by any body of scientific peers and should not be referenced in the open literature.

ABSTRACT

Predicting rib fractures remains an important challenge for the automotive safety community. While current rib computational models can successfully be used to determine the load and deflection required to cause rib fracture, they fail to properly predict the fracture location. It is assumed that a better understanding of bone fracture mechanism will help to improve the biofidelity of rib computational model. The goal of this study was to perform tensile tests of rib bone coupons to determine the fracture characteristics of the rib cortical bone. Thirty seven bone coupons were machined and tested under dynamic tensile load. An optical system was used to measure the in-plane displacements and strains on the outermost surface of each coupon. The Young's modulus, Poisson's ratio and failure strain were calculated based on the gathered data. An in-depth analysis of the strain distribution on the coupon surface was performed with the view to identify the fracture mechanisms. This study suggests that tension is not the main phenomenon that explains the onset of fracture in the rib cortical bone, and that properly predict rib bone fracture may require to account for the bone anisotropy and heterogeneity..

INTRODUCTION

Predicting rib fractures created by a dynamic event remains an important challenge for the automotive safety community and injury biomechanics at large. It is clear that the mechanical response of the human thorax can be greatly influenced by the number of fractured ribs. To determine rib injury mechanisms under dynamic loading the behavior of the ribs and the entire rib cage have been extensively investigated (Kent et al., 2004; Song et al. 2009; Shigeta et al., 2009; Lessley et al., 2010; Hallman et al. 2010). The rib bone material properties for bovine (Ferreira et al., 2006; Adharapurapu et al., 2006) and human bone (Keller et al., 1990; Kemper et al., 2005; Hansen et al., 2008; Subit *et al.*, 2011) have been reported by many researchers. The available data can be utilized to help to understand the rib mechanical behavior using modern engineering tools – e.g. finite element method (FEM) models. While current rib computational models can successfully determine the load and deflection required to cause the rib to fracture, they fail to properly predict the fracture location (Li et al., 2010). This indicates that further research is needed to

improve the knowledge of the fracture mechanisms in the rib, especially in its cortical bone. The cortical bone has voids and is a composite-like material that makes it non-homogenous. The bone material properties determined assuming homogeneity of the bone, are likely to inadequately describe the mechanical response of the rib. Therefore the goal of this study was to perform tensile tests of rib cortical bone coupons and analyze their deformation using a digital image correlation (DIC) method in order to determine the fracture characteristics of the rib cortical bone. A protocol was developed to machine and test rib bone coupons of constant thickness under dynamic loading. All the samples were imaged prior to testing using a micro-computed tomograph (microCT).

METHODS

The bilateral 6th and 7th ribs were harvested from three post mortem human subjects (PMHS; Table 1) in accordance with the ethical guidelines and research protocol approved by the Human Usage Review Panel and the University of Virginia institutional review board.

Table 1. PMHS information

Subject	Age at time of death	Couse of death	Body mass (kg)	Stature (cm)
510	69	Chronic obstructive pulmonary disease	93.4	168
511	49	Brain injury	98	175
518	70	Heart failure	67.6	165

Thirty seven bone coupons that were 25.4-mm long, 2.5-mm wide in the gage area, and 0.5 mm thick (fig. 1) were machined as it was described by Subit et al., 2013.

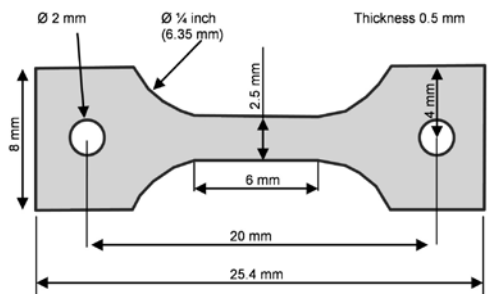

Figure 1: Dimensions of the rib cortical bone coupon

A hydraulic tensile machine (Model 8874, Instron Inc, Norwood, MA, USA), with a specially designed aluminum clamping system, was used to test the coupons under tensile loading (at constant velocity of 24 mm/s up to fracture). The clamping system consisted of two low-mass clamps (10.9 grams each, fig. 2). To prevent slippage of the coupon while avoiding bone crushing, a torque of 5 Nm was applied to the clamping screws prior to testing. The pins that go through the rod-end ball joints were utilized to connect the clamps to the base of the tensile machine and the end of the piston (fig. 3). After installing the clamps in the machine, all the samples were preloaded (between 1 N and 4 N) to ensure that there was no clearance between the pins and the clevises.

Figure 2: Detailed view of the clamps

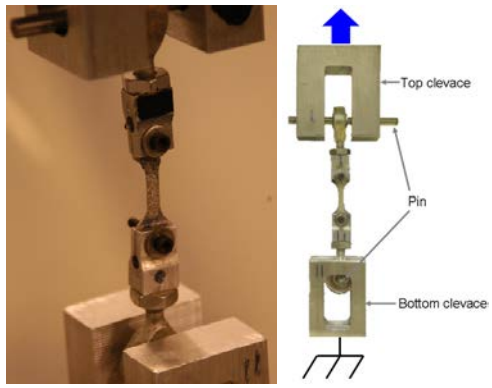

Figure 3: Clamping system for the coupons

The tensile load was measured by a three axis loadcell (model 6085, Denton Inc, Plymouth, MI, USA) located underneath the bottom clamp, connected to a standard data acquisition system (DEWE-2010, Dewton GmbH, Gratz, Austria). The displacement of the top clamp with reference to the tensile machine base was measured using a displacement potentiometer. The load and displacement were sampled at 100 kHz.

An optical system was used to measure the in-plane displacements and strains of each coupon (Aramis, GOM, Germany). The bone coupons were stored in a saline solution until the black-and-white paint pattern (fig. 4a) was applied to the outermost surface of the coupon. The optical system was comprised of one high-speed imager (NAC GX-1, NAC Image Technology, Simi Valley, CA) with a 100 mm macro lens. The average strains (ε_{11} and ε_{12}; fig. 4b) in the coupon gage area were calculated based from the Aramis results, and the tensile stress was estimated by dividing the tensile force by the cross-sectional area of the coupon gage area. The Young's modulus, Poisson's ratio and failure strain were also calculated. The (effective) Young's modulus was defined as the slope of the stress-strain curve between 0 and 0.5%. The bone microstructure and porosity were analyzed based on the microCT images, with the use of the MATLAB software (The Mathworks, Natick, MA, USA), and an in-depth analysis of the strain distribution on the coupon surface was performed with the view to identifying the fracture mechanisms.

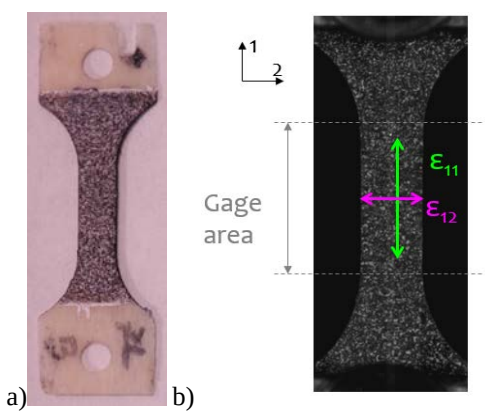

Figure 4: Coupon with a black-and-white pattern

RESULTS

The fracture occurred in the gauge area for 25 of the thirty seven coupons. For eight coupons the fracture occurred between the clamps and the gauge area. Four coupons broke within the clamping area. Based on the analyzed data, the test results were divided into three groups. When the fracture occurred in the gauge area and the stress-strain curve maintained a regular/smooth shape until fracture, the test was called

“good” (fig. 5a). When the fracture happened inside the gauge area, but in the stress-strain curve unexpected peaks/disturbances appeared, the test was called “not sure” (fig. 5b). If the specimen fractured outside the gauge area or the obtained stress-strain curve was highly distorted, the test was called “bad” (fig. 5c). From thirty seven tests 23 were reported as “good” tests, 7 as “not sure” and 7 as “bad”.

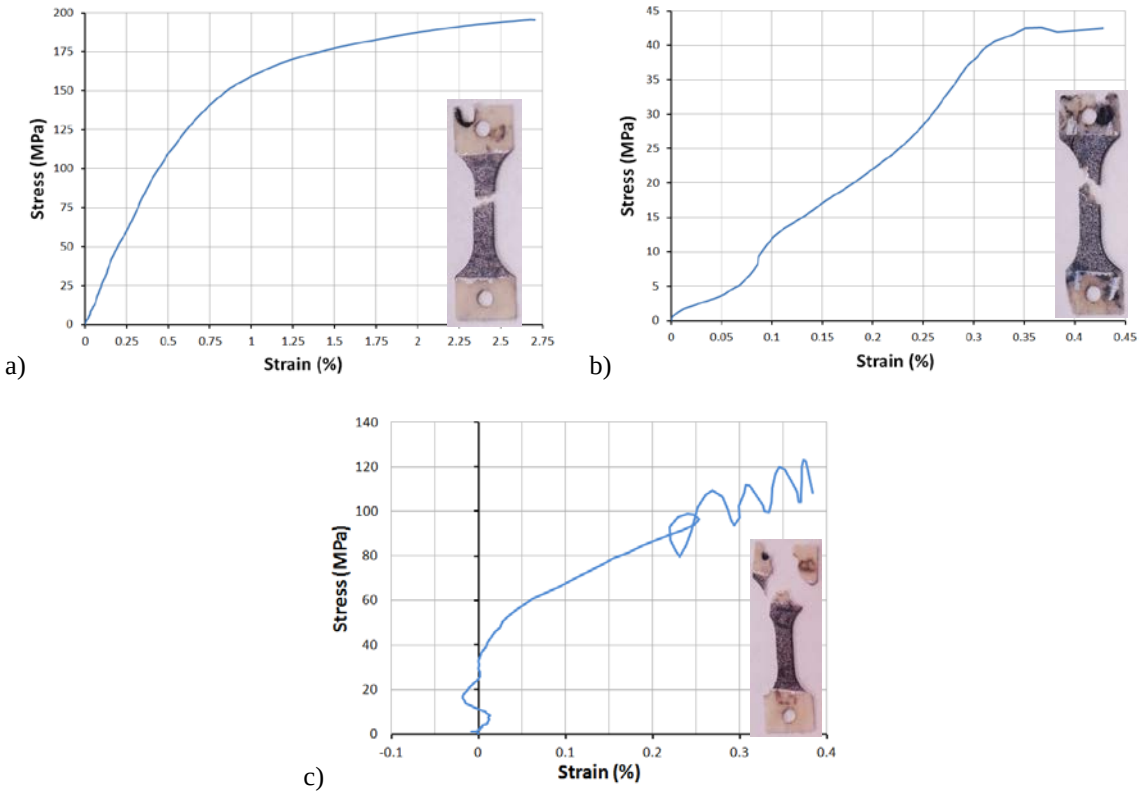

Figure 5: Example of a) “good” test; b) “not sure” test; c) “bad” test

Stress-strain curves for the good tests were plotted in fig. 6. For up to 0.5 to 0.75% of tensile strain, the rib bone characteristic could be approximated using a line with a slope representing the effective Young’s modulus of the material. After 0.75% of strain the curve slope decreased. After this point – called further a “yield point” – and until fracture, the material stress-strain tensile response could be described with a linear model using another slope. A bilinear model was used to describe the cortical bone behavior in the whole presented range. It is worth underlining that the material behavior after the yield point could not be called “plasticity”. During the tests it was not verified if the rib cortical bone maintains permanent deformation after unloading.

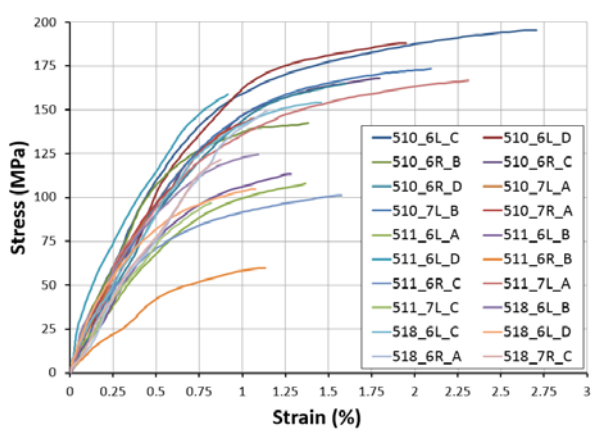

Figure 6: Material curves for “good” tests

The cortical bone material properties obtained from the “good” tests were as follows: Young’s modulus between 8.45 and 23 GPa, failure strain between 0.82 and 2.7 %, Poisson’s ratio between 0.14 and 1.05 (fig. 7; Appendix A).

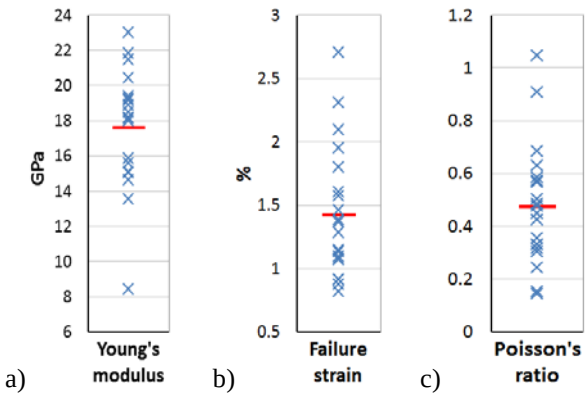

Figure 7: Material properties distribution within the “good” tests; red bar – mean value

Using the ARAMIS software an analysis of the displacement and strain distribution on the outermost surface of each coupon was performed. In case of the “good” test shown as an example in fig. 8, the actual maximum displacement in the X direction (referred to as X-displacement, fig. 8b) as well as the minimum strain in the X direction (referred to as X-strain, fig. 8d) indicated the fracture start point. The Y-displacement (fig. 8c) gradually increased from 0 (bottom coupon end attached to the base of the tensile machine) to 0.334% (top end attached to the piston). The Y-strain distribution (fig. 8e) indicated that despite a tensile load was applied to the coupon, tension was not the main type of loading that occurred in the coupon during the test. The Y-strain distribution in the gauge area did not correspond directly to the gradually increasing Y displacement.

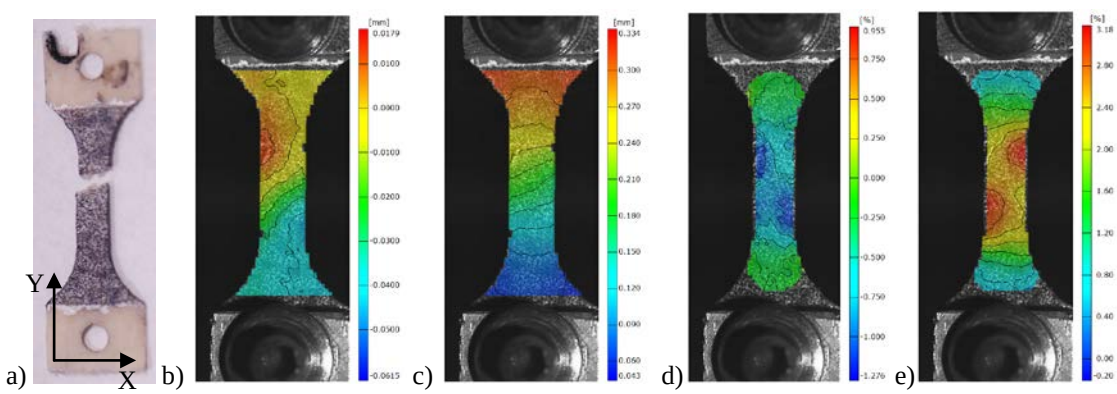

Figure 8: Example of “good” test: a) coupon with fracture; b) X displacement just before fracture; c) Y displacement just before fracture; d) X strain just before fracture; e) Y strain just before fracture

In case of the “not sure” test (fig. 9), the maximum displacement and strain (along both, X and Y axes) were reported in the vicinity of the fracture start location.

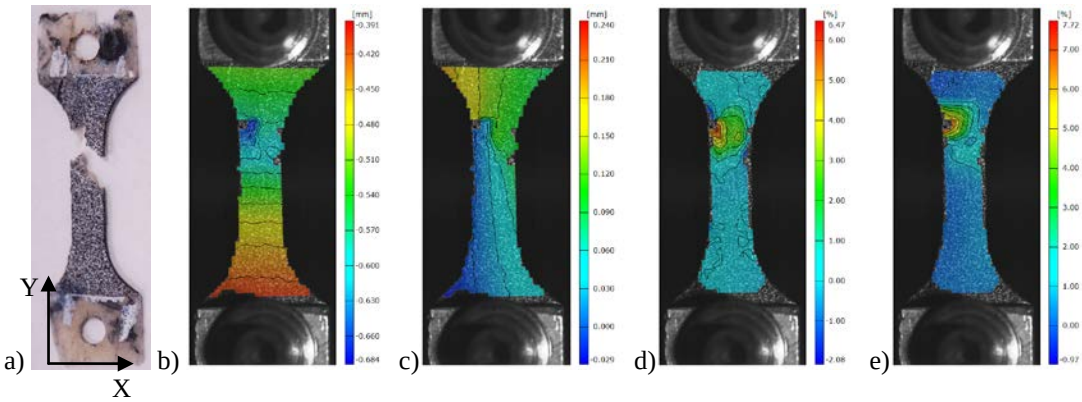

Figure 9: Example of “not sure” test: a) coupon with fracture; b) X displacement just before fracture; c) Y displacement just before fracture; d) X strain just before fracture; e) Y strain just before fracture

The effective cross-section area was calculated along the coupon for all the samples, but no correlation could be established between the location of the fracture and the cross-section area, which indicates that fracture was not caused only by tensile strain. In addition, the orientation of the principal strains at the fracture site was found to be coupon dependent, and the major principal strain was not always aligned with the longitudinal (tensile) direction of the coupon (fig. 10).

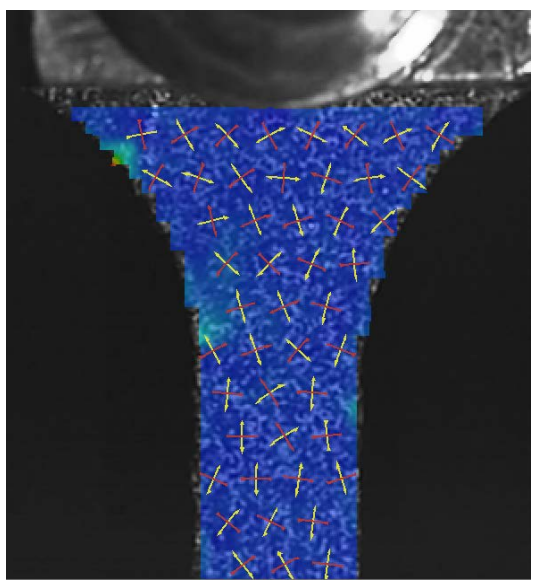

Figure 10: Orientation of the principal strains at the fracture site for one of the coupons (a few milliseconds before fracture). In yellow: major strain, in red: minor strain

At least four different types of fracture were reported in the current study. Most of the coupons, which broke in the gauge area, fractured in the transverse (X) direction (fig. 11a). The angle of the fracture line for those coupons (with regard to the X-axis) was between 0 and 45 degrees. Some coupons generated more irregular fracture shape, where the fracture line went in the transverse direction first and then the line followed the Y-axis, to switch back to the transverse direction in the end (fig. 11b). The third mechanism was observed for the coupons that broke between the gauge area and the clamping area, producing “V shape-like” fractures (fig. 11c). The shape of this fracture indicated that the main fracture mechanism was dictated by shear strain. This type of fracture was also previously reported in Subit et al., 2011. The fourth type of fracture occurred in the clamping area where one of the coupon flat ends was destroyed (fig. 11d) due to material imperfections (voids) or to a clamping force that was too low, which allow the extremity of the coupons to slip between the clamps.

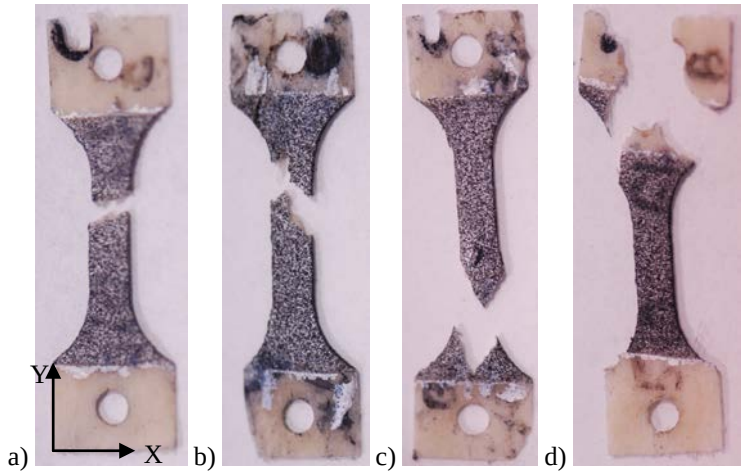

Figure 11: Four types of fracture observed in the study

DISCUSSION

Several different material models could be used to describe the cortical bone behavior, e.g. a simple bilinear model (mentioned before), more advanced piecewise linear model or a model taking viscoelasticity into account. However, due to the lack of information how the rib bone behaves after unloading (permanent deformation/nonlinear elasticity/hysteresis etc.), all these models could predict different injury thresholds/outcome for the same loading condition. Without further research focused on this phenomenon building a computational model of the rib or rib cage to predict injury can be very challenging.

The described experimental protocol was used previously to determine the material characteristics for the long bones – femur and tibia (Subit et al., 2013). While the Young's modulus for the rib bone and the lower extremities bones was in the same range (approximately 20 GPa) the rib bone exhibited much more nonlinear behavior (fig. 12). In addition, the failure strains determined for the rib bone in the current study were found to be significantly higher (up to almost 2.7% compering to approximately 1.25% for the tibia and 0.9% for the femur). The long bones exhibited a reponse that was nearly linear and brittle. The rib bone on the contrary was more ductile. This dissimilarity could be caused by differences in the microstructure of these bones. The long bone microstructure was nearly homogeneous, while in the case of the rib bone, more heterogeneity (more voids, gaps and irregularities) may explain the nonlinear behavior that was observed.

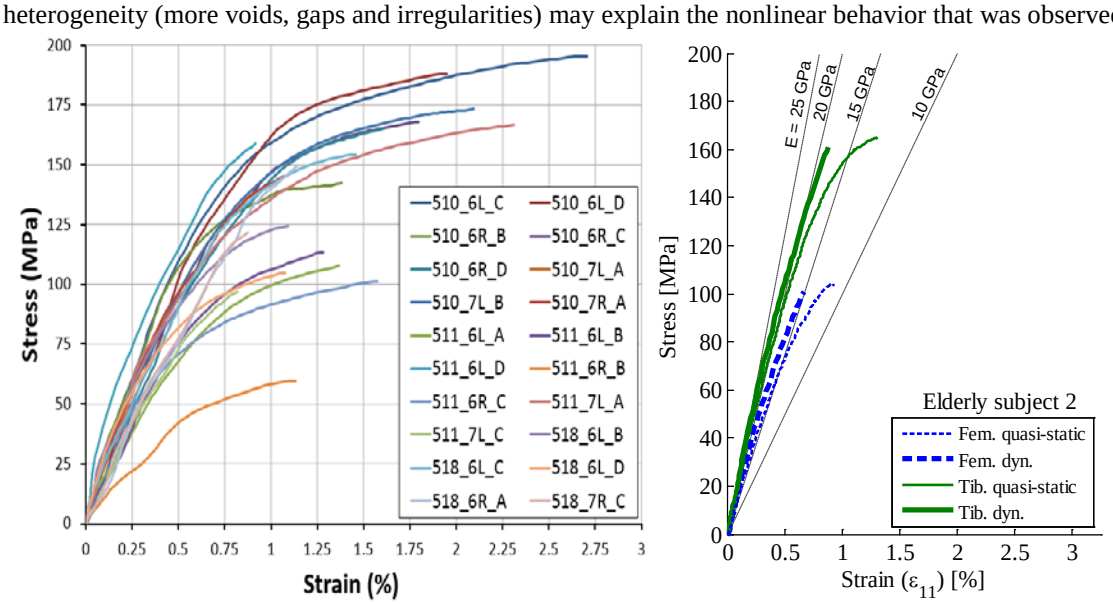

Figure 12: Comparison between material curves for the rib bone (left; "good tests") and the long bones (right, from Subit *et al.*, 2013)

During the processing of the experimental data, it was noticed that the design of the clamps could allow for the initial torsion or bending of the coupons or their out-of-plane alignment, which could influence the specimen behavior during a test. Due to the use of one high-speed camera, only the in-plane motion of the coupons could be tracked. Therefore the initial misalignments of the specimens as well as the motion of the superior clamp relative to the inferior clamp could not be captured properly and the effect of this relative motion on the mechanical response of the coupons was not fully investigated.

CONCLUSIONS

This study illustrates that the tension is not the main phenomenon that explains the occurrence of fracture in the rib cortical bone, and that material models that include the heterogeneity of the bone structure may be needed to properly predict fracture. Further analysis of the data generated in this study (strain distribution, microCT images) thanks to numerical methods such as inverse finite element method is expected to provide new insights about the fracture mechanisms in the rib bone. Such knowledge will ultimately contribute to improving the injury prediction capabilities of the thorax computational models commonly used in impact biomechanics.

REFERENCES

ADHARAPURAPU, R. R., JIANG, F., VECCHIO, K. S., (2006). Dynamic fracture of bovine bone. Materials Science and Engineering, C 26, 1325-1332.

FERREIRA, F., VAZ, M., SIMOES, J., (2006). Mechanical properties of bovine cortical bone at high strain rate. Materials Characterization, 57, 71-79.

HALLMAN, J.J., YOGANANDAN, N., PINTAR, F.A., (2010). Biomechanical and Injury Response to Posterolateral Loading from Torso Side Airbags. Stapp Car Crash Journal, 54, 227-257.

HANSEN, U., ZIOUPOS, P., SIMPSON, R., CURREY, J., HYND, D., (2008). The effect of strain rate on the mechanical properties of human cortical bone. J Biomech Eng 130.

KELLER, T., MAO, Z., SPENGLER, D., (1990). Young's modulus, bending strength, and tissue physical properties of human compact bone. Journal of orthopedics research, 8, 592-603.

KEMPER, A. R., MCNALLY, C., KENNEDY, E. A., MANOOGIAN, S. J., RATH, A. L., NG, T. P., STITZEL, J. D., SMITH, E. P., DUMA, S. M., MATSUOKA, F., (2005). Material properties of human rib cortical bone from dynamic tension coupon testing. Stapp Car Crash Journal, 49, 199-230.

KENT, R., LESSLEY, D., SHERWOOD, C., (2004). Thoracic response to dynamic, non-impact loading from a hub, distributed belt, diagonal belt, and double diagonal belts. Stapp Car Crash Journal 48, 495-519.

LESSLEY, D. J., SALZAR, R., CRANDALL, J., KENT, R., BOLTON, J. R., BASS, C. R., GUILLEMOT, H., FORMAN, J. L., (2010). Kinematics of the thorax under dynamic belt loading conditions. International Journal of Crashworthiness, 15, 175-190.

LI, Z., KINDIG, M., SUBIT, D., KENT, R., (2010). Influence of mesh density, cortical thickness and material properties on human rib fracture prediction. Medical Engineering & Physics, 32, 998-1008.

SHIGETA, K., KITAGAWA, Y., YASUKI, T., (2009). Development of next generation human fe model capable of organ injury prediction, 21st ESV Conference proceedings. Paper 09-0111.

SONG, E., TROSSEILLE, X., BAUDRIT, P., (2009). Evaluation of thoracic deflection as an injury criterion for side impact using a finite elements thorax model. Stapp Car Crash Journal, 53, 155-91.

SUBIT, D., DEL POZO DE DIOS, E., VELAZQUEZ-AMEIJIDE, J., ARREGUI-DALMASES, C., CRANDALL, J., (2011). Tensile material properties of human rib cortical bone under quasi-static and dynamic failure loading and influence of the bone microstructure on failure characteristics. arXiv: 1108.0390v1 [physics.bio-ph]

SUBIT, D., ARREGUI-DALMASES, C., SALAZAR, R., CRANDALL, J., (2013). Pediatric, Adult and Elderly Bone Material Properties. 2013 IRCOBI Conference Proceedings, Paper IRC-13-87

APPENDIX A – material properties from the good tests

COUPON ID	Young's modulus (GPa)	Poisson's ratio	Failure strain (%)	Porosity*
510-6L-C	21.82	0.3	2.7	0.029
510-6L-D	20.44	0.33	1.95	0.222
510-6R-B	21.48	0.63	1.38	0.071
510-6R-C	18.14	0.42	1.8	0.129
510-6R-D	18.1	0.14	1.6	0.165
510-7L-A	19.37	0.59	0.91	0.076
510-7L-B	19.17	0.48	2.09	0.342
510-7R-A	19.23	0.35	1.07	0.132
511-6L-A	13.54	0.31	1.37	0.090
511-6L-B	15.02	0.57	1.28	0.334
511-6L-D	23.01	0.91	0.91	0.492
511-6R-B	8.45	0.45	1.13	0.146
511-6R-C	15.86	0.5	1.58	0.246
511-7L-A	18.88	0.48	2.31	0.150
511-7L-C	14.61	0.33	0.82	0.093
518-6L-B	17.98	0.57	1.09	0.061
518-6L-C	18.16	0.68	1.46	0.100
518-6L-D	18.47	1.05	1.08	0.178
518-6R-A	15.08	0.15	1.15	0.228
518-7R-C	15.57	0.24	0.87	0.203
MAX	23.01	1.05	2.70	0.492
MIN	8.45	0.14	0.82	0.029
MEDIAN	**18.15**	**0.46**	**1.32**	**0.148**
MEAN	**17.62**	**0.48**	**1.43**	**0.174**
STD	**3.33**	**0.23**	**0.52**	**0.113**

* – “0” means no voids, “1” means no bone

APPENDIX B – material curves for “not sure” and “bad” tests

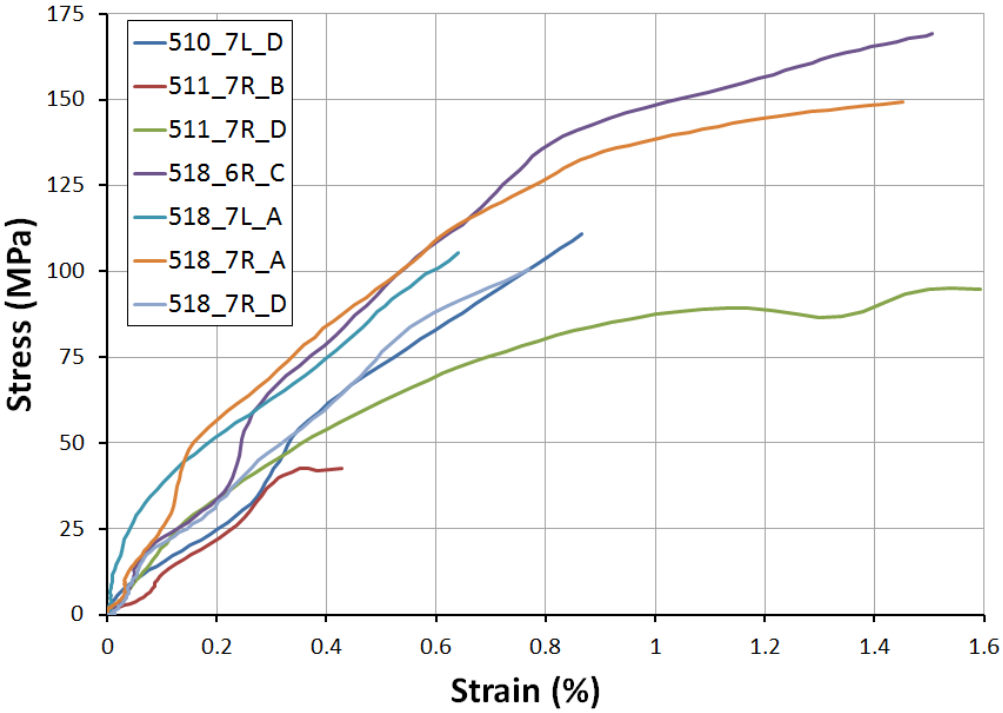

Figure 13: Material curves for “not sure” tests

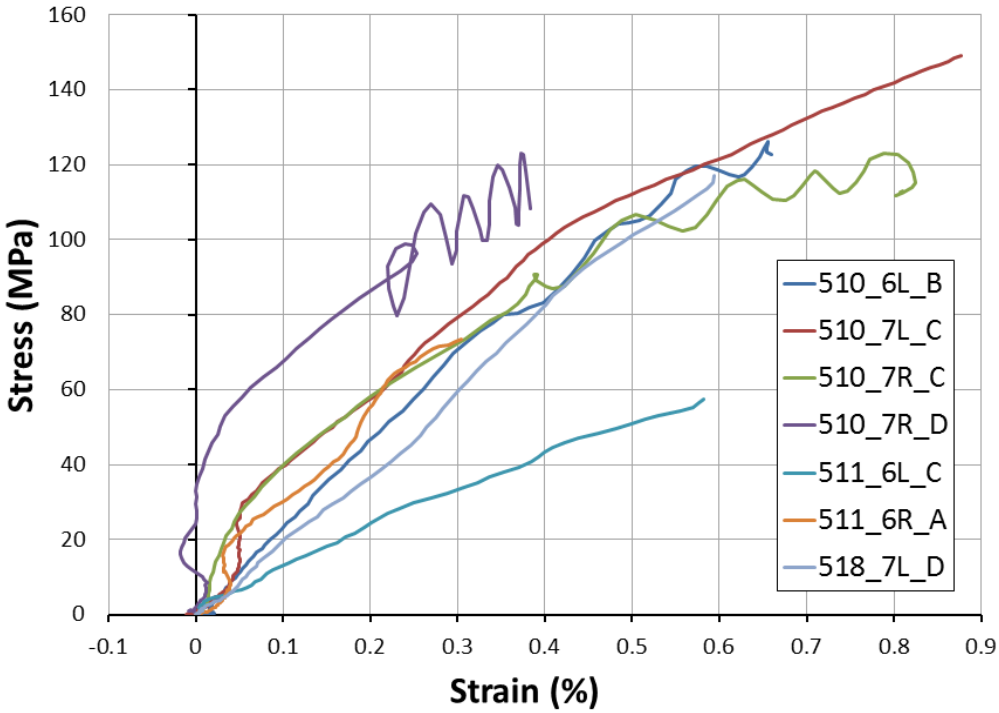

Figure 14: Material curves for “bad” tests